Final Report

Submitted to SPIRE Corporation
June 15, 2002

Epitaxial GaAs Neutron Detectors, Pixel Neutron Detector Arrays, and Compensated Pixel Detector Arrays

Douglas S. McGregor, Kansas State University

Raymond T. Klann, J.D. Sanders, Argonne National Laboratory

Holly K. Gersch, University of Michigan

Section A: General Detector Concept

1. Introduction

Since neutrons hold no electronic charge, methods used to recognize neutron interactions within a detector generally rely on second order effects. Two very common neutron interactions that are used for a variety of thermal neutron detectors are the $^{10}B(n,\alpha)^{7}Li$ reaction and the $^{6}Li(n,\alpha)^{3}H$ reaction [1-4] (see Figure 1).

The $^{10}B(n,\alpha)^{7}Li$ reaction leads to the following reaction products [1-4]:

$$^{10}\mathrm{B} + {}^{1}_{0}\mathrm{n} \rightarrow \begin{cases} {}^{7}\mathrm{Li}\,(\mathrm{at}\,1.015\,\mathrm{MeV}) + \alpha\ (\mathrm{at}\,1.777\,\mathrm{MeV}), & 2.792\ \mathrm{MeV}(\textit{to ground state}) \\ {}^{7}\mathrm{Li}^{*}(\mathrm{at}\,0.840\,\mathrm{MeV}) + \alpha\ (\mathrm{at}\,1.470\,\mathrm{MeV}), & 2.310\ \mathrm{MeV}\,(\textit{1st excited state}) \end{cases}$$

(Reaction Q– Value)

which are released in opposite directions when thermal neutrons (0.0259 eV) are absorbed by ^{10}B. After absorption, 94% of the reactions leave the ^{7}Li ion in its first excited state, which rapidly de-excites to the ground state (~10^{-13} seconds) by releasing a 480 keV gamma ray. The remaining 6% of the reactions result in the ^{7}Li ion going directly to its ground state. The microscopic thermal neutron absorption cross section is 3840 barns. Additionally, the microscopic thermal neutron absorption cross section decreases with increasing neutron energy, with a dependence proportional to the inverse of the neutron velocity ($1/v$) over much of the energy range [5,6].

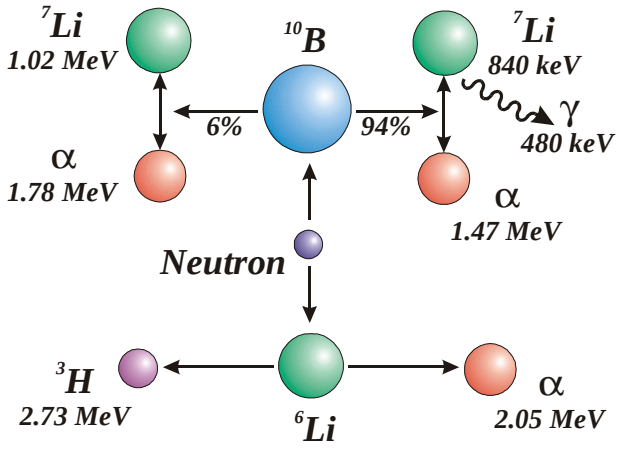

Figure 1: The two most commonly used neutron reactions for thermal neutron detection purposes are the $^{10}B(n,\alpha)^{7}Li$ reaction and the $^{6}Li(n,\alpha)^{3}H$ reaction.

The $^{6}Li(n,\alpha)^{3}H$ reaction leads to the following products:

$$^{6}\mathrm{Li} + {}^{1}_{0}\mathrm{n} \rightarrow {}^{3}\mathrm{H}\,(\mathrm{at}\,2.73\,\mathrm{MeV}) + \alpha\ (\mathrm{at}\,2.05\,\mathrm{MeV}), \qquad 4.78\ \mathrm{MeV}$$

(Reaction Q– Value)

which again are oppositely directed if the neutron energy is sufficiently small. The microscopic thermal neutron (0.0259 eV) absorption cross section is 940 barns. The thermal neutron absorption cross section also demonstrates a $1/v$ dependence, except at a salient resonance above 100 keV, in which the absorption cross section surpasses that of ^{10}B for energies between

approximately 150 keV to 300 keV [5,6]. Additional resonances characteristic to either isotope cause the absorption cross section to surpass one or the other as the neutron energy increases. Due to its higher absorption cross section, the $^{10}B(n,\alpha)^{7}Li$ reaction leads to a generally higher reaction probability than the $^{6}Li(n,\alpha)^{3}H$ reaction for neutron energies below 100 keV. However, the higher energy reaction products emitted from the $^{6}Li(n,\alpha)^{3}H$ reaction lead to greater ease of detection than the particles emitted from the $^{10}B(n,\alpha)^{7}Li$ reaction.

There are other neutron reactions that have been used in solid-form films for thermal neutron detectors, including the $^{157}Gd(n,\gamma)^{158}Gd$ reaction [7-11] and the $^{113}Cd(n,\gamma)^{114}Cd$ reaction [12,13], both of which have very large thermal neutron reaction cross sections. The $^{157}Gd(n,\gamma)^{158}Gd$ reaction leads to the emission of various low energy gamma rays and beta particles, most of which are emitted at energies below 220 keV. The appeal of using ^{157}Gd is due to its large thermal neutron cross section of 240,000 barns [5,6], but the resulting low energy conversion electron and gamma ray emissions can be difficult to distinguish from background gamma rays in a high radiation field. Furthermore, purified ^{157}Gd is expensive. Natural Gd is a viable alternative since its natural abundance of ^{157}Gd is 15.7%, which still yields an overall thermal neutron absorption cross section of 46,000 barns. The ^{113}Cd reaction is useful as well, with its thermal neutron absorption cross section of 20,000 barns [5,6]. Discreet gamma ray emissions from the $^{113}Cd(n,\gamma)^{114}Cd$ reaction extend beyond 9 MeV, however the salient gamma ray emissions are at 558.6 keV and 651.3 keV [14,15], which can be discerned with a relatively high resolution gamma ray spectrometer. Unfortunately, any gamma ray spectrometer capable of detecting the $^{113}Cd(n,\gamma)^{114}Cd$ emissions will also detect any other background gamma rays, which can confuse the measurement.

The neutron detector design discussed in the present work consists of a solid-state detector (or semiconductor diode detector) coated with a solid form of neutron reactive material. Such a device has been often described as a “foil coated” neutron detector, although we adapt the more descriptive name of thin-film-coated neutron detector. Only ^{10}B- and Gd-based neutron reactive coatings were used in the presented work.

2. The Basic Concept

Thin film neutron detectors consist of semiconductor diodes, preferably with very thin contact layers, upon which a layer (or layers) of neutron reactive material has been deposited. The basic concept has been used by a variety of research groups [16-28]. As shown in Figure 2, neutrons absorbed in the neutron reactive film release charged particle reaction products in opposite directions, one of which may enter the semiconductor diode detector. Charged particles entering the detector lose their energy through Coulombic scattering, thereby creating a high-density plasma cloud of columnar ionization in the form of electron-hole pairs. The semiconductor diode detector is voltage biased to separate the electron-hole pairs and drift the charges to their respective contacts. The mobile charges each induce an image charge on the contacts as they move through the device, and the induced charge is integrated and measured by an external preamplifier and accompanying electronics.

It is important to note that the charged particles have discrete ranges within a material, and they lose energy as a function of the specific “stopping power” of the material through which they pass [29]. Charged particle energy loss is not linear with distance, and the energy loss for non-relativistic high-energy charged particles can generally be described by the Bethe-Bloche stopping power relation [30]

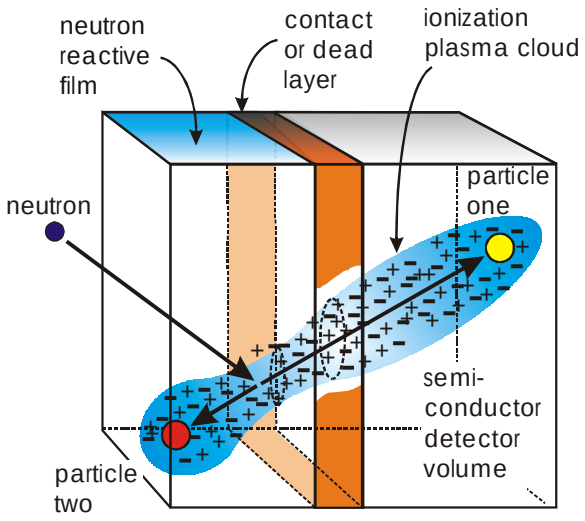

Figure 2: The fundamental approach to a thin-film-coated semiconductor neutron detector. The film thickness should not exceed the maximum range of the "long range" reaction product. The reaction products are emitted in opposite directions.

$$s = -\frac{1}{N}\frac{dE}{dx} = \frac{4\pi z^2 q^4}{m_o v^2} Z \ln\left(\frac{2m_o v^2}{J}\right), \tag{1}$$

where zq and v are the charge and the velocity of the charged particle, N is the atomic density, m_o is the rest mass of an electron, Z is the material atomic density, and J is an experimentally determined quantity describing the average excitation potential of a representative atom in the material. Although the average range is treated as constant, the actual range fluctuates from particle to particle due to deviations in the number of Coulombic scatters per unit distance and deviations in energy loss per collision. The fluctuation may exceed 5% of the total range, and the deviation is referred to as the "straggle" in the particle range. In the unique case of protons, alpha particles, and other relatively low mass heavy ions, the energy loss as a function of distance can be described by the Bragg ionization curve, in which [29]

$$I(r) = \int_0^\infty \frac{i(x-r)}{\beta\sqrt{\pi}} e^{-[(x-R)/\beta]^2} dx \ , \tag{2}$$

where x is the range of the individual particle, r is the distance that the particle has traveled in the material, i $(x - r)$ is the specific ionization along the path of the ionizing particle at point $(x - r)$ from the end of its path, R is the mean range and β is the straggling parameter. An interesting characteristic of the Bragg ionization curve for alpha (α) particles is the increase in columnar ionization per unit volume as the ion energy decreases. Hence, the highest density of electron-hole pairs are excited near the end of the range for α-particles. In the present treatment the *average effective range* (denoted L) is the distance through which a particle may *travel within the neutron reactive film* before its energy decreases below the set minimum detectable threshold, typically defined by the electronic lower-level-discriminator (*LLD*) setting. The term does not take into account additional energy losses from contact "dead regions." L_{SR} and L_{LR} denote the average effective ranges for the short-range and long-range reaction products, respectively.

Neutrons may interact anywhere within the reactive film. From Figure 2, it is apparent that the reaction products will also lose energy as they move through the reactive film, thus limiting the energy transferred to the semiconductor detector. The finite specific energy loss in the reactive film limits the usable film thickness that can be deposited over the semiconductor device. The voltage signal measured is directly proportional to the number of electron-hole pairs created within the semiconductor. Reaction products that deposit most or all of their energy in the semiconductor volume will produce much larger voltage signals than those reaction products that lose most of their energy in the surface films and contacts.

The neutron flux transmitted through the film as a function of distance x can be described by [31]

$$I(x) = I_0\, e^{-x\sigma_F N_F} = I_0\, e^{-x\Sigma_F} \quad , \tag{3}$$

where I_0 is the initial neutron flux, N_F is the atomic density of the neutron reactive *isotope* in the film, σ_F is the microscopic thermal neutron absorption cross section of the film, and Σ_F is the film macroscopic thermal neutron absorption cross section. It is apparent that the fraction of neutrons absorbed in the film through distance x is

$$1 - \frac{I(x)}{I_0} = 1 - e^{-x\sigma_F N_F} = 1 - e^{-x\Sigma_F} \quad , \tag{4}$$

The neutron absorption probability per unit distance is described by [20]

$$p(x)dx = \Sigma_F\, e^{-x\Sigma_F}\, dx \quad . \tag{5}$$

The angular contribution to self-attenuation must also be addressed. Once a neutron is absorbed and the reaction products are emitted, the probability that a reaction product particle will enter the detector is determined by the solid angle subtending the surface within the average effective range (L) of the particle interaction. From Figure 3, a neutron interaction taking place at distance x from the semiconductor surface has a probability of entering the active volume as described by the fractional solid angle that subtends the detector,

$$p_p(x) = \frac{\Omega(x)}{4\pi} = \frac{2\pi}{4\pi}\left(1 - \frac{x}{L}\right) = 0.5\left(1 - \frac{x}{L}\right), \qquad x \le L\,, \tag{6}$$

where the subscript p relates to the reaction product particle of interest. Since the reactions of interest in the present work release two different reaction products per event, the total probability of detecting a neutron reaction consists of adding the detection probabilities of both reaction products. Note that it is possible that only one reaction product may be able to reach the semiconductor active volume. Figure 4 demonstrates the variation in detection efficiency for different neutron interaction depths. Interactions occurring near the detector contact result in either particle entering the detector with high probability. As the neutron interaction distance increases, the solid angle of the short-range particle decreases more rapidly than that of the long-range particle, resulting in an overall decrease in detection sensitivity. At neutron interaction distances greater than L_{LR}, the long-range particle can no longer reach the detector and the neutron absorptions are undetected. Ultimately, it serves no purpose to increase the thickness of the neutron reactive thin film beyond L_{LR}, as will be shown, and actually works to decrease the overall neutron detection efficiency.

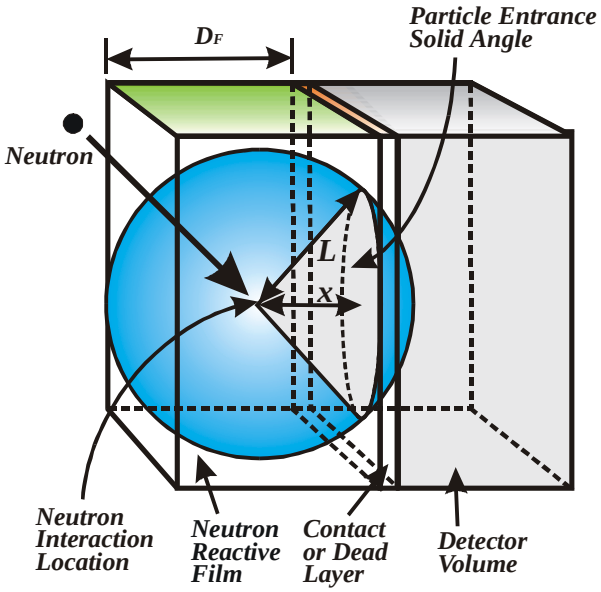

Figure 3: The solid angle formed by the reaction product ranges that subtends the detector at the interface predetermines the detection probability.

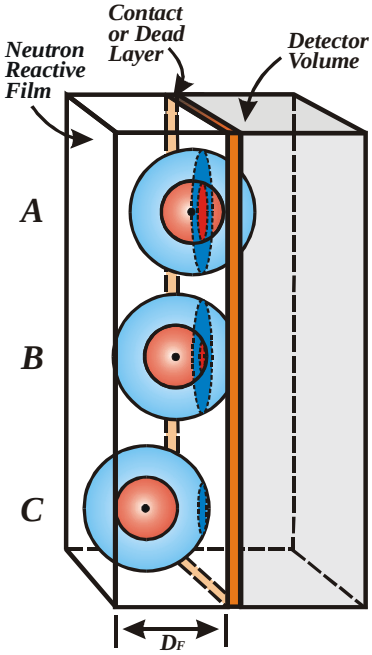

Figure 4: The solid angle subtending the detector at the interface is greatest for reactions occurring at the film/detector interface. Show are cases where (A) either particle may enter the detector with high probability, (B) the short range product has diminished detection probability, and (C) the short range product will not be detected and the long range product has diminished detection probability.

a. Front Side Irradiation - The Uniformly Coated Planar Case

A commonly used geometry involves the use of a planar semiconductor detector on which a neutron reactive film has been deposited. For such a device, the boundary conditions are:

i. The neutron reactive films coating the device are uniform and conformal.
ii. The device surface is void of morphological imperfections.
iii. The device plane is situated perpendicular to a neutron beam.
iv. The lateral dimensions of the detector are large compared to the maximum charge particle ranges within the reactive film.
v. The source neutrons are of low enough energy such that kinetic energy effects are negligible. In other words, the reaction products are emitted opposite each other at an angle of 180^{o}.

The coordinate system shown in Figure 5 is adapted for the following analysis. It is assumed that the contact thickness (D_1) is negligible. Equation 3 becomes

$$I(x) = I_0 \, e^{-\Sigma_F (D_F - x)}, \tag{7}$$

where D_F is the converter film thickness and I_o is the initial neutron beam intensity before entering the reactive film. Additionally, Equation 5 becomes

$$p(x)dx = \Sigma_F \, e^{-\Sigma_F (D_F - x)} \, dx \ . \tag{8}$$

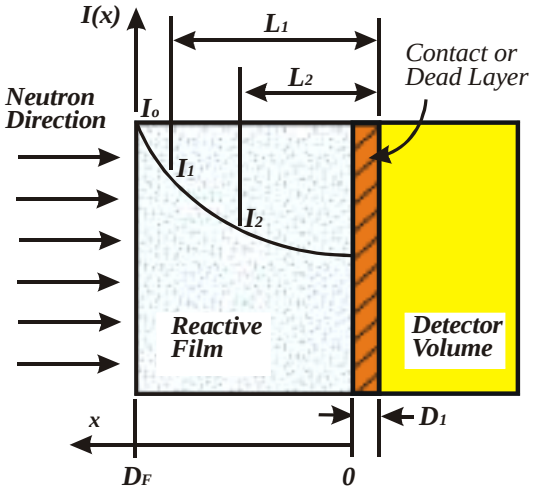

Figure 5: Coordinate system for front irradiation of coated neutron detectors.

The sensitivity contribution for a reaction product particle can be found by integrating over the product of the interaction probability (Equation 7) and the fractional solid angle through film thickness D_F:

$$S_p(D_F) = \frac{F_p}{4\pi I_0}\int_0^{D_F} I_0\, 2\pi\Sigma_F\, e^{-\Sigma_F(D_F-x)}\left(1-\frac{x}{L}\right)dx$$
$$= 0.5F_p\left\{\left(1+\frac{1}{\Sigma_F L}\right)\left(1-e^{-\Sigma_F D_F}\right)-\frac{D_F}{L}\right\} \quad , \tag{9a}$$

for $D_F \le L$, and

$$S_p(D_F) = \frac{F_p\, e^{-\Sigma_F(D_F-L)}}{4\pi I_0}\int_0^{L} I_0\, 2\pi\Sigma_F\, e^{-\Sigma_F(D_F-x)}\left(1-\frac{x}{L}\right)dx$$
$$= 0.5\, F_p\, e^{-\Sigma_F(D_F-L)}\left\{\left(1+\frac{1}{\Sigma_F L}\right)\left(1-e^{-\Sigma_F L}\right)-1\right\} \quad , \tag{9b}$$

for $D_F > L$, where F_p refers to the branching ratio of the reaction product emission. The total sensitivity can be found by adding all of the reaction product sensitivities, hence

$$S(D_F)\big|_{Total} = \sum_{p=1}^{N} S_p(D_F) \quad , \tag{10}$$

where N is the number of different possible reaction products. In the case of ^{10}B-based films N equals 4, whereas for ^{6}Li-based films N equals 2. Notice from Equation 9*b* that the value of S_p decreases as D_F becomes larger than the value of L. As a result, there will be an optimal neutron reactive film thickness for front irradiated detectors. Since the minimum particle detection threshold determines the average effective range (L), the optimal film thickness is also a function of the *LLD* setting.

The maximum neutron sensitivity from any particular charged particle reaction product can found by differentiating Equation 9*a* with respect to the film thickness D_F,

$$\frac{dS_p}{dD_F} = \frac{d}{dD_F}\left[0.5F_p\left\{\left(1+\frac{1}{\Sigma_F L}\right)\left(1-e^{-\Sigma_F D_F}\right)-\frac{D_F}{L}\right\}\right] = 0.5F_p\left\{\left(\Sigma_F+\frac{1}{L}\right)e^{-\Sigma_F D_F}-\frac{1}{L}\right\}, \tag{11}$$

where the local maxima is found by setting Equation 11 to zero. For a particular charged particle reaction product p, the film thickness that allows for the maximum detection efficiency is

$$D_F\big|_{p\max} = \frac{1}{\Sigma_F}\ln\left(\Sigma_F L+1\right) \quad . \tag{12}$$

Figure 6 shows the value of $D_{F(pmax)}$ as a function of the $\Sigma_F L$ product. As shown, at small values of $\Sigma_F L$, the value of $D_{F(pmax)}$ is approximately equal to the value of L. When all reaction products are included, the optimal film thickness is determined by taking the derivative of Equation 10. The process becomes complicated by the need to select the appropriate equation, either Equation 9*a* or 9*b*, for each of the reaction products. For the sake of illustrating the behavior of the system, some appropriate assumptions can be made. In a two-product system, the

long-range particle can be assumed to dominate. Hence, the derivative of Equation 9*a* is used for the long-range particle and the derivative of Equation 9*b* is used for the short-range particle. Continuing with such a theme, for multiple particle systems (as with $^{10}B(n,\alpha)^{7}Li$), we use Equation 9*a* for the longest-range particle, and Equation 9*b* for the remaining particles. It can therefore be shown that

$$D_F\big|_{\max} = \frac{1}{\Sigma_F}\ln\left[\left(\Sigma_F L_{LR}+1\right)-\frac{L_{LR}}{F_{LR}}\sum_{p=2}^{N}\Psi_p\right] \quad , \tag{13}$$

where the subscript *LR* refers to the longest range reaction product, *N* is the total number of different reaction products, and

$$\Psi_p = F_p\Sigma_F e^{\Sigma_F L_p}\left[\left(1+\frac{1}{\Sigma_F L_p}\right)\left(1-e^{-\Sigma_F L_p}\right)-1\right] \quad , \tag{14}$$

which represents the remaining shorter range charged particle reaction products. For a two-particle system in which the reaction products differ in mass, Equations 13 and 14 are reliable. However, with a multiple-particle system, the branching ratios may dictate that a shorter-range particle actually dominates the maximum achievable sensitivity, in which case Equation 13 will not yield the correct optimal film thickness. In such cases, the optimal film thickness can be found by iteratively solving Equation 10 for the maximum calculated efficiency and corresponding film thickness. Regardless, the Σ*L* product remains an important parameter in determining the optimum neutron reactive film thickness.

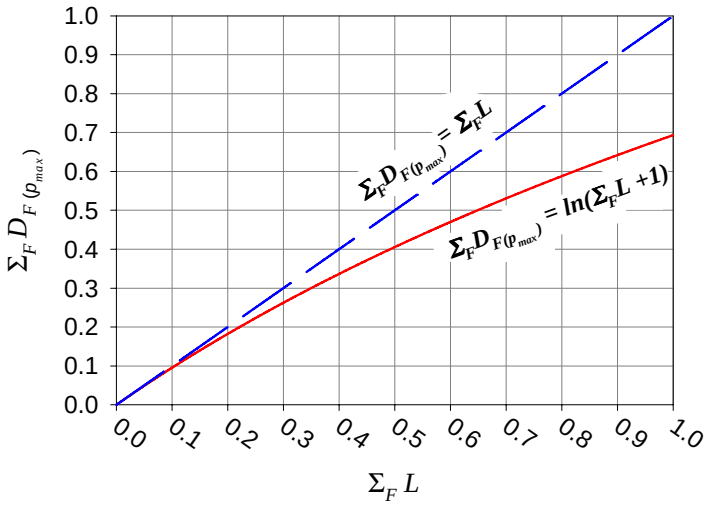

Figure 6: Comparison of optimized ^{10}B thickness for front and back-irradiated detectors as a function of Σ and *L*.

It is important to note from Figure 5 that, for front side irradiation, the highest neutron interaction rate within the film is the farthest distance from the film-detector junction. Additionally, the lowest neutron flux and corresponding interaction rate is adjacent to the film-detector junction, and the rate decreases as the film thickness increases.

Overall, the front-coated device operates as a neutron counter. In order to discriminate against background gamma rays, the energy discriminator should be set high enough to reduce the probability of mistaking a gamma ray event for a neutron event. Figures 7 and 8 show the expected thermal neutron detection efficiency for ^{10}B, ^{6}LiF, and ^{6}Li films as a function of thickness (D_F) with an *LLD* setting of 300 keV. The ^{10}B film has the lowest efficiency, peaking at approximately 4% detection efficiency. However, the ^{10}B film thickness required to achieve 4% efficiency is only 2.4 microns, whereas comparable efficiencies for pure ^{6}Li and ^{6}LiF layers require 12 microns and 18 microns of material, respectively. Only a marginal gain in efficiency can be achieved with ^{6}LiF, peaking at approximately 4.4% thermal neutron detection efficiency at a film thickness of 26 microns. Pure ^{6}Li offers the highest achievable efficiency, peaking at 11.5% efficiency for a film thickness of 100 microns. Although pure ^{6}Li may appear attractive as a relatively efficient thermal neutron detection film, the fabrication, handling and packaging issues render detector production much more difficult than that required for ^{10}B or ^{6}LiF-coated devices. Additionally, other schemes can increase the efficiency of ^{10}B- or ^{6}LiF- coated devices.

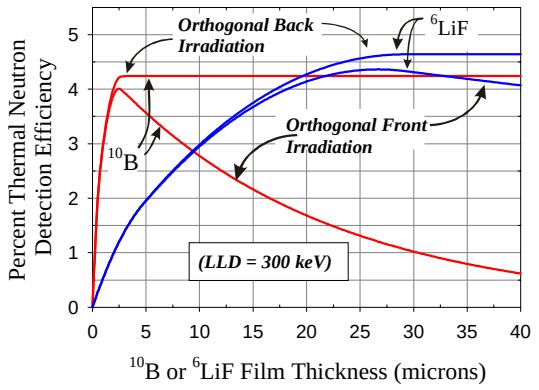

Figure 7: The calculated thermal neutron detection efficiencies for front and back irradiation as a function of film thickness for ^{10}B- and ^{6}LiF-coated detectors.

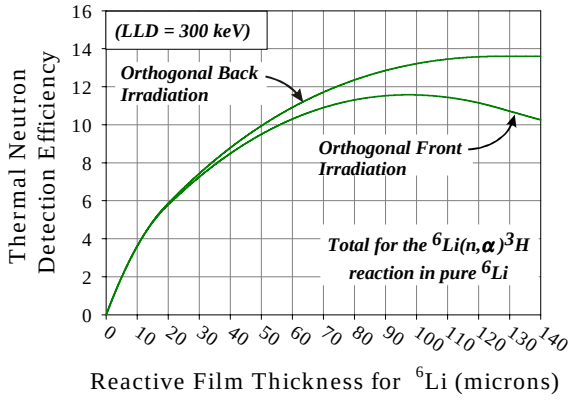

Figure 8: The calculated thermal neutron detection efficiencies for front and back irradiation as a function of film thickness for pure ^{6}Li-coated detectors.

b. Backside Irradiation

To eliminate the dependence of the optimum film thickness on the *LLD* setting, the thin film coated neutron detector can be designed to operate via backside irradiation. The geometry of such a device is depicted in Figure 9. Notice that neutron absorption can take place in the detector before reaching the reactive film, and these losses must be accounted for by incorporating Equation 3 for each layer. Hence, the neutron intensity reaching the reactive film can be represented by

$$I\big|_{\text{interface}} = I_0 \prod_{i=1}^{M} e^{-\Sigma_i D_i}\,, \tag{15}$$

where Σ_i is the macroscopic cross section for each layer, D_i is the thickness of each layer, and M is the number of detector layers *excluding* the thermal neutron reactive film. Assuming orthogonal backside irradiation, the sensitivity contribution for each particle is determined by integrating the product of Equations 5 and 6 over the film thickness D_F. Hence, we have

$$S_p(D_F) = \frac{F_p}{4\pi I_0} I_0 \prod_{i=1}^{M} e^{-\Sigma_i D_i} \int_0^{D_F} 2\pi\Sigma_F \, e^{-x\Sigma_F} \left(1 - \frac{x}{L}\right) dx$$

$$= 0.5 F_p \prod_{i=1}^{M} e^{-\Sigma_i D_i} \left\{ \left(1 - \frac{1}{\Sigma_F L}\right)\left(1 - e^{-\Sigma_F D_F}\right) + \frac{D_F}{L} e^{-\Sigma_F D_F} \right\} \quad , \quad D_F \le L \qquad (16a)$$

and

$$S_p(D_F) = \frac{F_p}{4\pi I_0} I_0 \prod_{i=1}^{M} e^{-\Sigma_i D_i} \int_0^{L} 2\pi\Sigma_F \, e^{-x\Sigma_F} \left(1 - \frac{x}{L}\right) dx$$

$$= 0.5 F_p \prod_{i=1}^{M} e^{-\Sigma_i D_i} \left\{ \left(1 - \frac{1}{\Sigma_F L}\right)\left(1 - e^{-\Sigma_F L}\right) + e^{-\Sigma_F L} \right\} \quad , \quad D_F > L \qquad (16b)$$

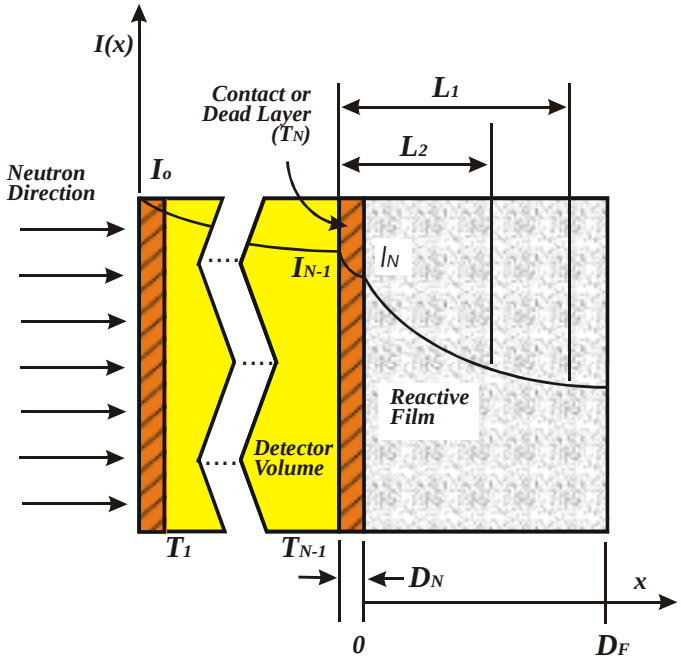

Figure 9: Coordinate system for back irradiation of coated neutron detectors.

Contrary to the front irradiation case, the lowest neutron interaction rate within the reactive film is the farthest distance from the film-detector junction, and the highest neutron interaction rate within the reactive film is adjacent to the film-detector junction (Figure 9). As a result, the backside irradiated devices can achieve slightly higher neutron sensitivities than front side irradiated devices (Figures 7 and 8). To use the backside irradiation scheme effectively, the semiconductor detector layers should be very thin and composed of materials with relatively small neutron interaction cross sections. Otherwise, significant neutron losses will occur before they can reach the reactive film, thereby undermining the advantage of backside irradiation. The total neutron sensitivity can be found by employing Equations 10 and 16.

Section B: Detector Designs and Configurations

1. Basic Pixel Detector Arrays

The main pixel detector design incorporated for the present work is a dual in-line array of 0.5 mm x 1.0 mm rectangular Schottky diodes fabricated from bulk semi-insulating (SI) GaAs material. The devices were fabricated in the same manner as described in the section C.1. with the exception that the detectors consisted of long dual in-line arrays. Each individual pad is coated with ^{10}B and has its own small wire bond pad for electrical connection (see Figure 10). A 50-micron gap separates each pixel from its immediate neighbor, hence removing the problem of cross–talk. The pixel design allows for several small detectors to be operated simultaneously so as to gather a digitized image of neutron interactions in the device plane. The linear arrays were designed to extend completely across the GaAs wafers. Hence, the linear array can be sliced to any length thereby allowing for arrays ranging from 8 pixels up to 256 pixels in a single device.

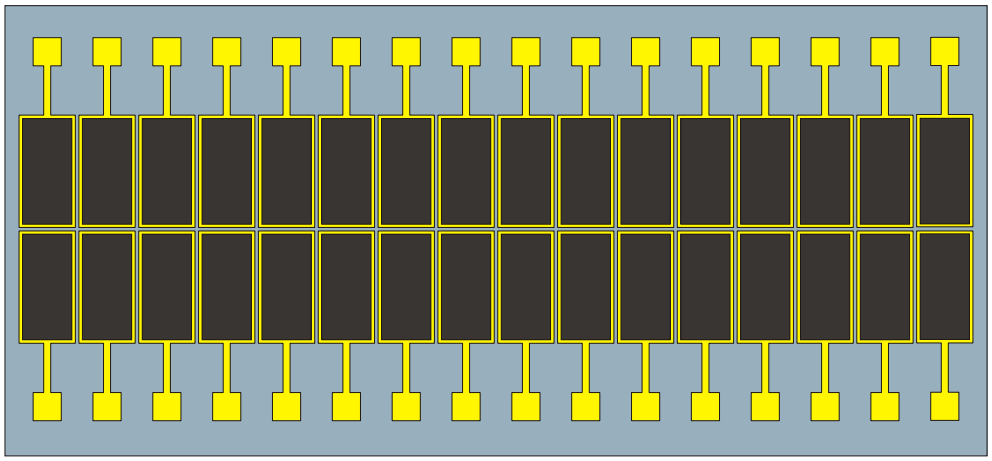

Figure 10: A depiction of a 32-pixel dual in-line array, the typical size used in the present work.

The pixel devices were Ag-epoxied to common chip carriers and wire bonded to the pin-outs (see Figure 11). The chip carriers selected plug into a custom socket produced for the project. The socket was hard-wired into an aluminum box were 16 individual miniaturized preamplifiers were wired to a selected side of the socket (see Figure 12). The aluminum box serves several purposes:

i. Aluminum has a very low interaction cross section for neutrons, hence will not interfere with the neutron imaging measurements.
ii. The light impenetrable aluminum box prevents photoelectric noise.
iii. The conductive sealed aluminum box shields from electromagnetic noise.

The Cremat model CR-101D was the preamplifier type chosen for the preliminary work. The devices have low noise and have a large enough dynamic range to accommodate the large signals expected from the coated neutron detectors. The preamplifiers were arranged in two stacks next to the GaAs array chip, and each preamplifier was capacitively coupled a pixel through the socket. The preamplifier stacks power inputs were connected in parallel, hence only *one power supply*, capable of supplying ± 9 volts, was required to operate the both stacks of preamplfiers. Output signals were extracted through LIMO connectors to standard NIM electronics (described elsewhere).

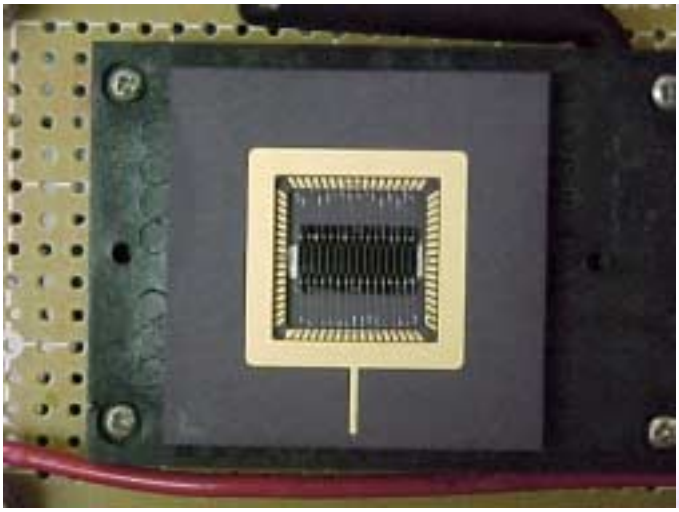

Figure 11: A 32-pixel dual in-line ^{10}B-coated bulk GaAs Schottky barrier array fastened and packaged in the chip carrier.

Figure 12: The 32-pixel dual in-line ^{10}B-coated bulk GaAs Schottky barrier array located in the aluminum testing box with the accompanying electronics.

2. Self-biased Detectors

The "self-biased" radiation detector design incorporates a thin high purity semiconductor region, ranging from 1 to 6 microns thick, grown upon a bulk substrate. Placed atop the high purity region a blocking contact that is either a thin semiconductor or a Schottky contact. The internal potential formed by the potential difference in the work function of the blocking contact and the high purity region provides enough voltage to operate the device. In the present work, the self-biased detectors were manufactured from n-type GaAs substrates. High purity ν-type GaAs epitaxial layers were grown on the GaAs substrates, over which blocking contacts were fabricated. Due to the thinness of the epitaxial layers, only ^{10}B-coated devices and Gd-coated devices were manufactured, primarily because ^{6}Li(n,α)^{3}H reaction products (from ^{6}LiF and ^{6}Li layers) would transit well beyond the 6 micron layer and deposit most of their energy within the substrate (insensitive) region.

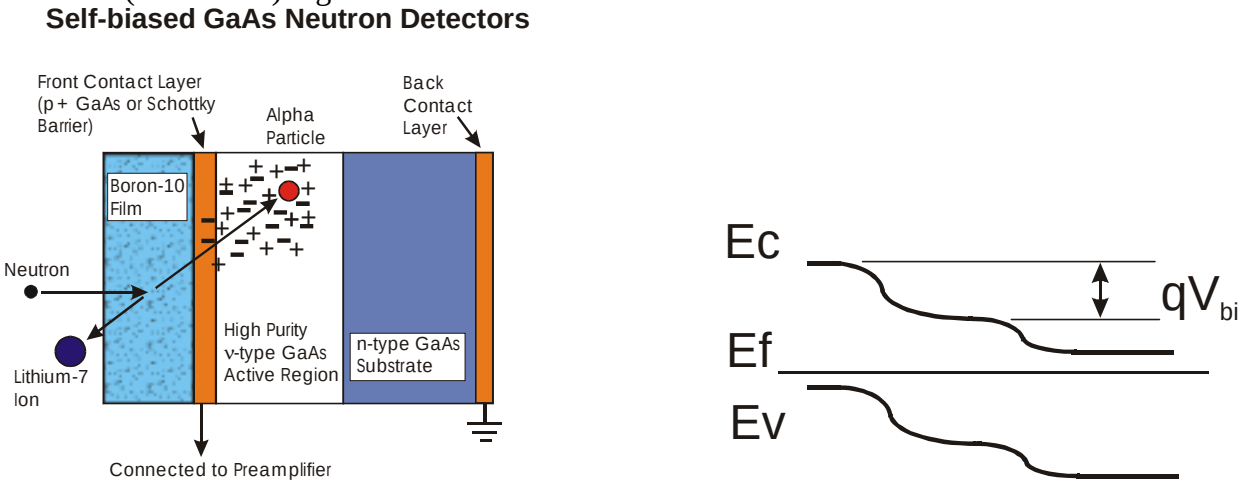

Figure 13: The basic construction of a ^{10}B-coated self-biased high-purity epitaxial GaAs neutron detector. Neutrons interact in the ^{10}B film, thereby releasing an alpha particle and a ^{7}Li ion in opposite directions. Only one particle from the interaction can enter the detector. The built-in potential at the contact/ν-type GaAs interface supplies enough voltage to operate the device.

Two basic diode structures were investigated, both of which incorporated high-purity undoped GaAs epitaxial layers grown onto *n*-type GaAs substrates. The undoped GaAs regions had background impurity concentrations of $n = 3x10^{14}/cm^3$, yielding ν-type unintentionally-doped GaAs material. Two blocking contact adaptations were applied to the high-purity ν-type GaAs regions: 2000 Å thick *p*+ GaAs blocking contacts and 200 Å thick Schottky blocking contacts. Six variations of these structures were fabricated. The *p*+ contact and high-purity ν-type epitaxial GaAs films were grown by low-pressure metalorganic chemical vapor deposition. The ν-type GaAs active layers ranged between 1 micron and 5 microns in thickness. The device sensitive areas were 3mm x 3mm, each coated with a 1.5mm diameter film of 98% enriched high-purity ^{10}B. Two variations were coated with 6500 Å of ^{10}B, one with 7200 Å of ^{10}B, and three with 5000 Å of ^{10}B. The detector elements were bonded to common T0-5 headers and tested for thermal neutron sensitivity in custom designed, light impenetrable aluminum boxes. The difference between the work functions of the blocking contacts (*p*+ GaAs layers or Schottky contacts) and the ν-type high-purity GaAs layers produces an internal potential difference at the film interface [32]. The "built-in" potential produces an internal electric field. The internal electric field is strong enough to deplete a good portion of the ν-type GaAs region and transport a considerable fraction of the charge carriers excited by the charged particle across the active ν-type region. Therefore, external voltage bias is not required to operate the devices. Voltage need only be applied in order to operate the supporting readout electronics. The Schottky barrier devices demonstrated slightly higher reverse leakage currents than the *p*+ contact devices, an expected result due to the lower barrier height generally formed by Schottky contacts as compared to *p-i-n* structures. Furthermore, the built-in potential of the *p-i-n* structure is higher than the Schottky barrier structure due to the larger difference in work functions between the *p*+ region and the ν-type GaAs region, resulting in a higher internal electric field.

Energy self-absorption from ions crossing the 2000 Å *p*+ layer will ultimately reduce the amount of energy deposited directly in the detector. Assuming that electron-hole pairs excited in the *p*+ region do *not* contribute to the measured output signal, calculations indicate that energy lost from 840 keV ^7Li ions crossing the *p*+ region will range between 40 and 100 keV depending upon the particle trajectory and $^{10}B(n,\alpha)^7Li$ reaction location [33]. Additionally, the average energy lost from 1.47 MeV alpha particles crossing the *p*+ region will be 74 keV. Yet, such a view is somewhat pessimistic in that a significant portion of excited electrons can diffuse from the *p*+ region into the ν-type region whereupon they will be collected and contribute to the output signal. Regardless, the thin 200 Å Schottky barriers should have much less charge loss in the contact region than the *p*+ contact devices.

3. Self-biased Compensated Pixel Detectors Arrays

The self-biased compensated design incorporates a split pixel, in which half of the split pixel is coated with a neutron reactive coating while the other half remains bare. Hence, the coated portion is sensitive to both gamma rays and neutrons while the uncoated portion is sensitive to only gamma rays. Since both halves are identical in size, then they received the same amount of radiation exposure. The self-biased design allows for very low leakage current noise during operation, which assists in minimizing signal contamination during operation.

The device operates by simultaneously collecting data in a mixed radiation field on both pixel portions. During operation, the coated portion registers "positive" events, while the uncoated portion registers "negative" events. Hence, the negative count events are subtracted from the positive counts events, which yields the resulting neutron count sensitivity.

The device is designed to operate in “real time,” hence the image accumulates during operation and it is not necessary to take two separate measurements before subtracting the spectra. The method allows for a more accurate representation of the neutron transmission image since both pixel halves experience identical radiation exposure to gamma rays and neutrons, a case not necessarily true if separate counting measurements are taken. The device is designed to also work with Gd coatings, where the advantageous large neutron absorption cross section of Gd can be used while reducing the inconvenience of its low reaction product energies.

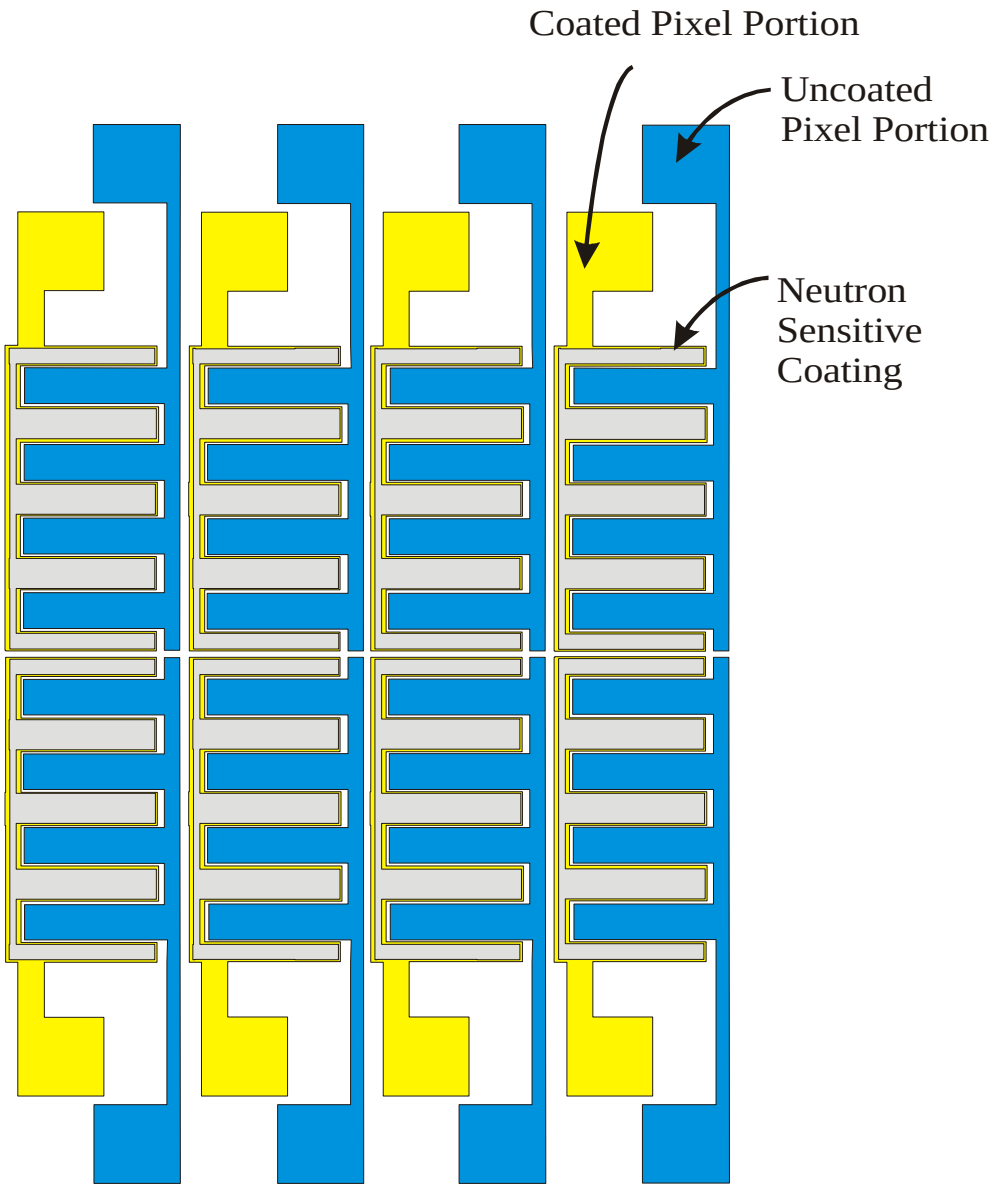

Figure 14: The split-pixel design used two inter-woven pixels. Both halves of the pixel are identical in size, with one coated with neutron reactive material and the other remaining uncoated.

Section C: Device Results

Neutron computed tomography (CT) techniques have been implemented as a method to determine the spatial distribution of nuclear material. One of the limiting factors in the development of these systems, however, has been detector response in the harsh radiation environment. Further, since SNF cannot be easily relocated, a portable system that can rapidly determine the spatial distribution of nuclear materials is desired.

Radiation hard neutron CT systems using gas detectors have been developed for the non-destructive analysis of SNF, but the limited spatial resolution of gas detectors restricts their applicability. Neutron CT systems based on CCD detectors have higher spatial resolution than gas-based systems, but the neutron conversion screen and mirror system currently used limits system portability. Solid state GaAs neutron detectors have been shown to be both radiation hard [34] as well as gamma ray insensitive [25,35], both advantageous properties in the SNF environment. Further, arrays of these detectors are relatively easy to assemble and the resulting detection system is much smaller than current CCD-based systems.

A neutron CT system based on a solid state GaAs neutron detecting array has been developed and tested. Presented in the following is a description of the system developed and resulting reconstructed images [36].

The neutron CT system developed consists of a GaAs neutron detector, sample platform capable of linear and rotary movement, computerized control and data acquisition system, and a filtered-backprojection CT reconstruction algorithm. A collimated thermal neutron beam was provided by E-port of the Ford Nuclear Reactor (FNR), and epithermal neutrons were provided by a Sb/Be photoneutron source. Transmission radiography of several phantoms was performed at multiple angles and used to reconstruct tomographic images.

1. Images
   a. GaAs Neutron Detectors

The detector developed for this system is composed of a 16x2 pixel array of ^{10}B-coated GaAs Schottky barrier detectors [25,35]. Each pixel has dimensions of 1 mm by 0.5 mm with 50 μm of insulation between the pixels to prevent cross talk. The detector is mounted on a 64-pin chip holder and housed in a light tight Al box to provide shielding from RF and visible light interference (Figures 11 and 12).

The thickness of the ^{10}B film used for this detector is 1 μm, resulting in a measured thermal neutron detection efficiency of 2.8%, matching well with theory [25]. Custom preamplifier circuits capable of measuring the energies deposited in the device from the $^{10}B(n,\alpha)^{9}Li$ reaction were developed and mounted within the Al box. The current detector only uses one row of the array, creating an 8.8 mm x 1 mm active area.

The design of the detector allows for discrimination between the signals produced from background gamma rays and those from neutrons by setting the lower level discriminator (*LLD*) at 300 keV for each pixel [35]. Radiation hardness studies previously mentioned have revealed that catastrophic damage occurs at fluence above 10^{13} n/cm^2 [34]. Pixel size of the current detector was chosen for ease of manufacturing and is ultimately limited by the range of charge particles in the neutron-absorbing medium. For boron-coated devices this is less than 5 μm [25,35]. Detector matrices with higher efficiency conversion layers and smaller pixels are currently being investigated.

The output from each channel was amplified using a Canberra 2022 amplifier and lower level discrimination performed using an Ortec 423 single channel analyzer (SCA). The *LLD* setting was determined by the system noise and gamma ray contribution from the beam. As shown elsewhere [25], setting the *LLD* to approximately 300 keV discriminates out much of the gamma-ray background. An Ortec Labmaster PC card was used as a multichannel counter, enabling automated data collection.

b. Sample Platform

The object to be imaged was placed on a sample platform with step motor controlled linear and rotational axes, both controlled via the serial port of a personal computer. For samples larger than the detector active area, the linear step motor was used to move the platform along the face of the detector. Future system improvements will include the addition of vertical platform motion to allow image acquisition of large objects

c. Neutron sources

Two neutron sources were used for the CT experiments presented, a thermal neutron beam from a nuclear reactor and an epithermal Sb/Be photoneutron source. The Sb/Be source is composed of an Sb cylinder surrounded by a Be sleeve and produces neutrons through a photoneutron reaction, resulting in a neutron distribution centered on 23 keV as well as a significant gamma-ray component [37,38].

The Sb/Be neutron source was chosen for its portability and neutron energy, which closely match the transmission peak of iron [3,4]. Future development will involve investigating the effects of placing an iron filter between the source and detector to filter background radiation from the SNF and scattered epithermal neutrons.

A collimator containing lead and borated polyethylene was placed between the sources and the phantom, as shown in Figure 15. This collimator limited the beam size to the active area of the detector, but was unpixilated. Experiments were also performed with a collimator placed between the sample and detector in order to assess the effects of neutron scattering within the sample.

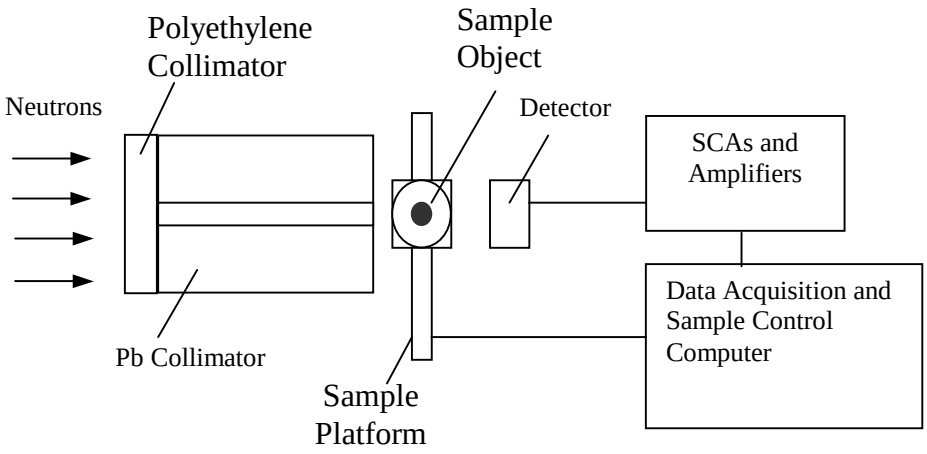

Figure 15: Neutron CT experimental setup with thermal neutron beam. A custom holder was developed to hold the Sb/Be photoneutron source.

d. Data Correction and Reconstruction

A set of transmission projection data was collected for each sample at multiple angles. Raw data from objects imaged in the thermal beam were corrected for fluctuations in reactor power and the profile of the beam by normalizing each profile to a profile taken without the object. Due to the decay of the Sb source, epithermal beam images were corrected to account for both the beam profile and the decay of the source. Before performing the reconstruction, the data was scaled to a range from 0 to 255 and arranged into a sinogram. A filtered-backprojection reconstruction algorithm utilizing several Fourier filters was used to map the spatial neutron attenuation recorded in the sinogram. A Shepp & Logan filter was used for all reconstructions.

e. Discussion

Several phantoms were developed to assess the quality of the system. The first sample investigated was an aluminum block containing several water columns of different diameter, as shown in Figure 16. This sample was placed in the thermal beam as close to the detector as possible. Since the object was much larger than the active area of the detector, the sample was walked across the face of the detector in increments of 6.6 mm. Figure 17 shows the neutron intensity along the sample. The steep intensity profile at the edges of the holes is one pixel wide, indicating that the pixel size is currently the major limit on spatial resolution.

The epithermal Sb/Be source was also used to image the aluminum block with water columns. At 23 keV the total macroscopic cross section of water is H_2O nearly the same as that of Al. As a result, images of the sample in the epithermal beam did not reveal the water columns.

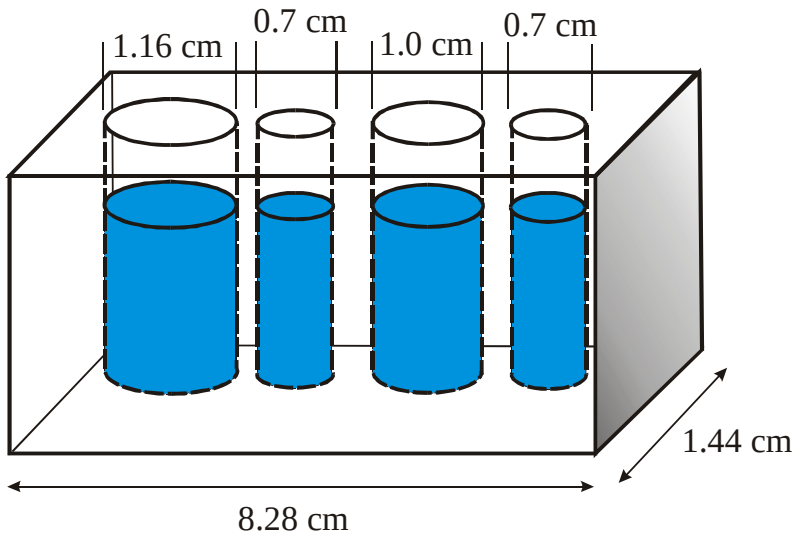

Figure 16: Schematic of Al block containing H_2O columns of various diameters used to determine spatial resolution.

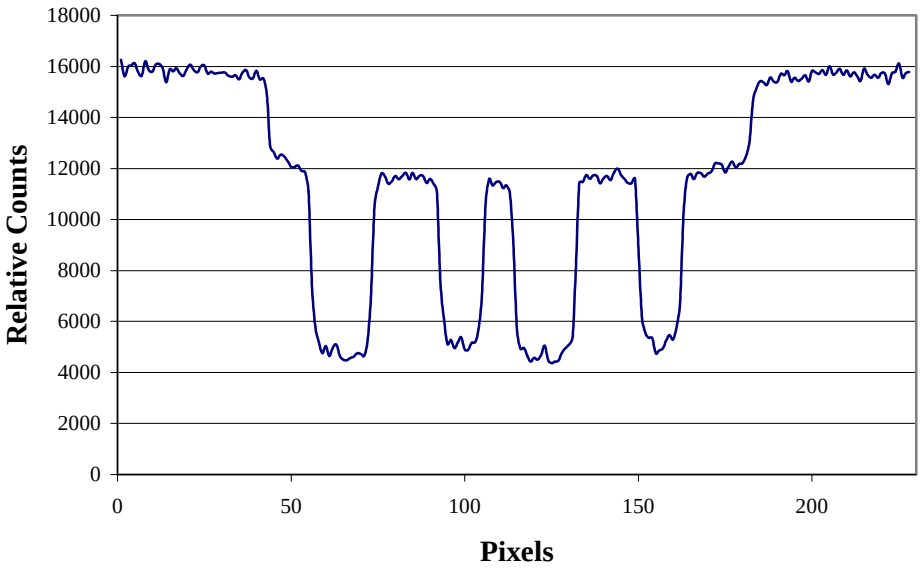

Figure 17: Thermal neutron intensity profile of Al block sample with water columns of various diameters. Resolution appears to be limited by pixel size.

Step wedge samples of Cu, Al, steel and polyethylene were imaged to characterize the ability of the system to differentiate the attenuation coefficients of the materials. These samples were placed as close to the detector as possible and again walked across the detector face in 6.6 mm increments. Except for the polyethylene sample, all six steps were easily discernable a neutron intensity plot (see Figures 18 through 21).

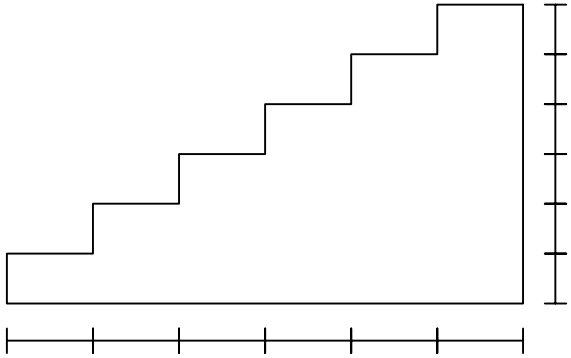

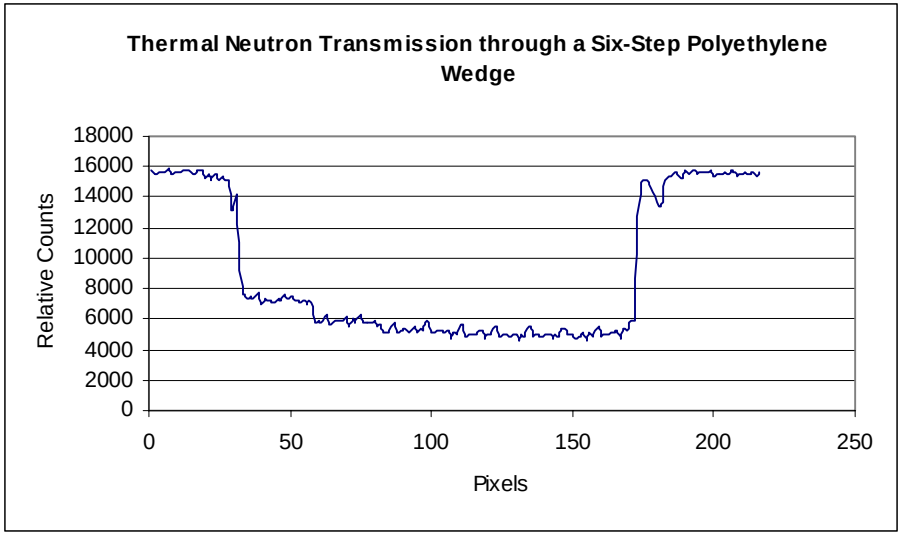

Figure 18: Polyethylene step wedge dimensions and results.

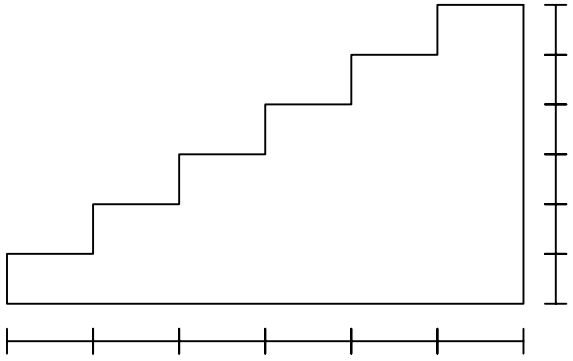

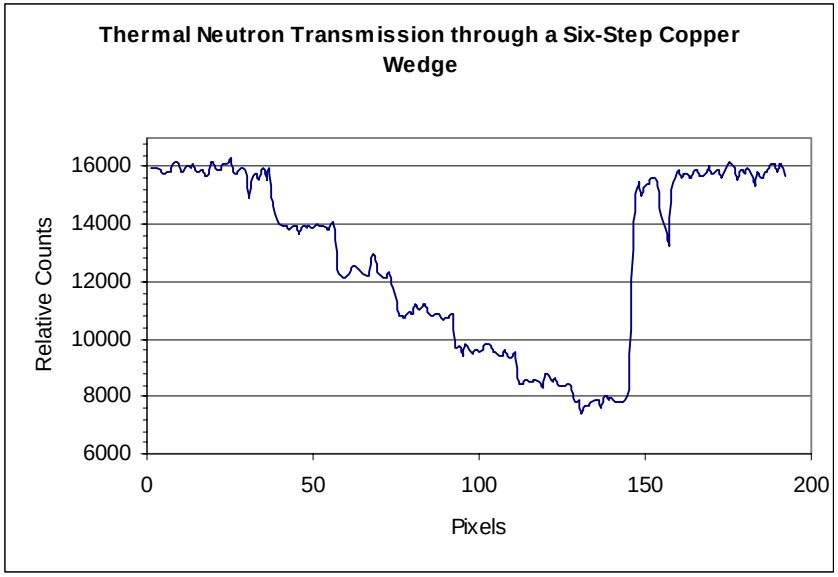

Figure 19: Copper step wedge dimensions and results.

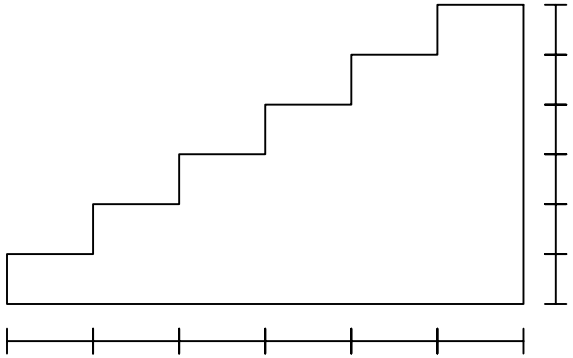

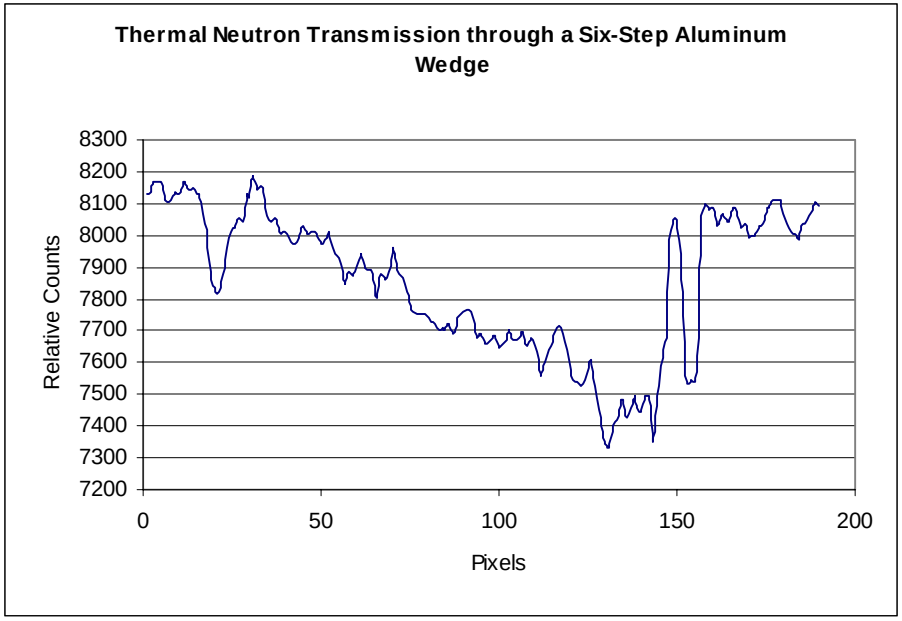

Figure 20: Aluminum step wedge dimensions and results.

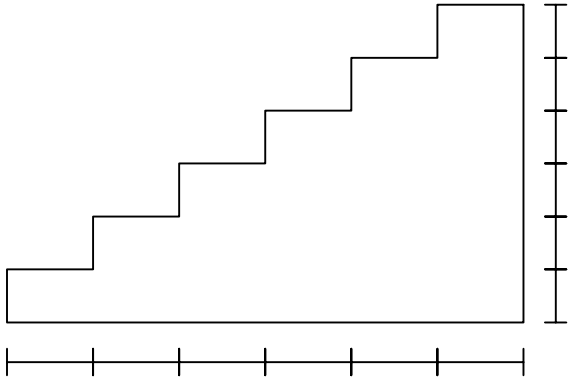

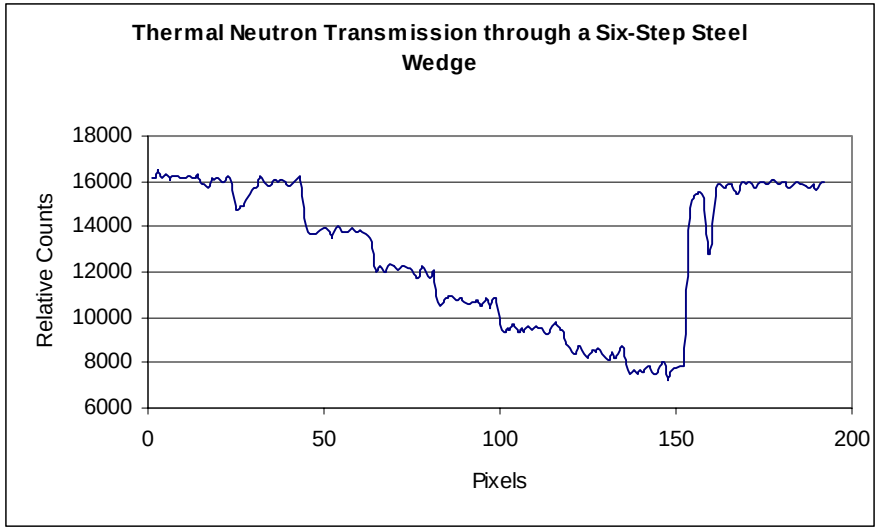

Figure 21: Steel step wedge dimensions and results.

As shown in Figure 22, a plot of the measured vs. accepted macroscopic cross section shows a non-linear relationship, making material determination difficult using the current setup. The disagreement between the measured cross section and accepted values is mainly due to scatter within the sample. Placing a pixilated collimator between the sample and detector is one method of decreasing this effect, while active measurements of the scattering effects can allow correction for the total scatter present, as shown in the literature [39]. The attachment of a pixilated collimator to the detector face is currently being investigated.

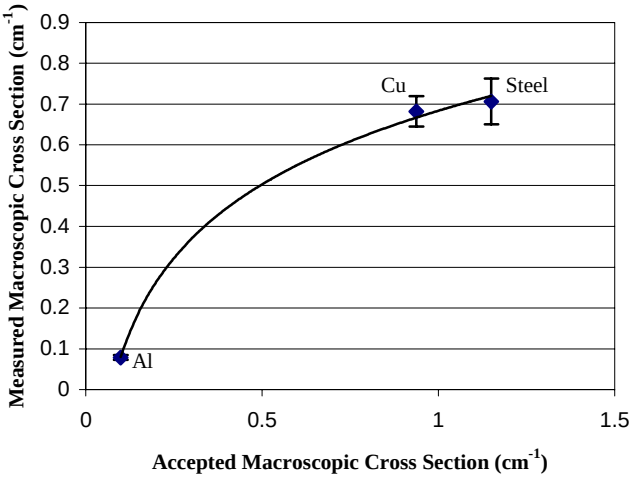

Figure 22: Plot of measured vs. accepted macroscopic cross section for Al, Cu and steel, demonstrating the non-linear response of the current setup.

Figure 23 shows the schematic drawing of a cylindrical sample placed in the thermal beam to characterize the tomographic system. In order to limit the effects of scatter within the sample, a non-pixelated Pb collimator was placed between the sample and the detector. The sample was rotated through 180 degrees in increments of 3 degrees, and 10-minute counts

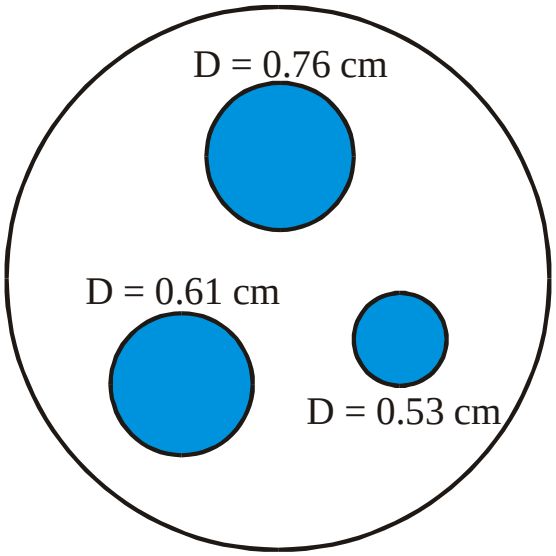

collected.

Figure 23: Schematic of Al cylinder sample containing water columns of different diameters.

Performing a filtered-backprojection reconstruction with a Shepp & Logan filter results in the image shown in Figure 24. An intensity threshold was applied the reconstructed image based upon the neutron transmission intensity profile of the sample. A threshold level of 50% of the maximum water column intensity was chosen, corresponding to a gray scale intensity of 115. As can be seen in Figure 25, all three water columns are clearly visible. The measured area of all three water columns is 0.78 cm^2, approximately 80% of that expected, indicating a decreased resolution to that found in the radiographic line image shown in Figure 17. This resolution decrease is expected due to the convolution used during the reconstruction process, which adds additional noise to each pixel. Experiments to determine the tomographic resolution of the system are currently bein

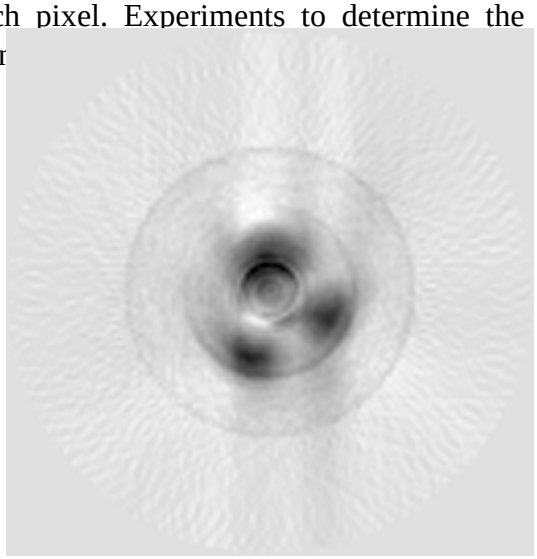

Figure 24: Reconstructed image of Al cylinder sample with a Shepp & Logan filter applied. Each pixel is 0.25 mm x 0.25 mm.

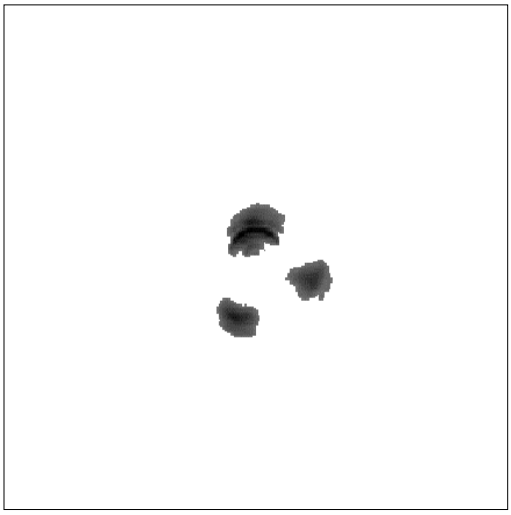

Figure 25: Reconstructed image of Al cylinder sample in thermal beam with a threshold value of 115. All three water columns are easily discernable and the measured area 80% of that expected.

The epithermal Sb/Be source was also used to image a cylindrical steel sample, shown in Figure 26. The sample was rotated through 180 degrees in increments of 5 degrees and 45 minute counts collected. Increasing the count time was necessitated by the decreased cross section of boron at 23 keV, lowering the detection efficiency from 2.8% to less than .001% [35]. The experimental setup was the same as used for the thermal reconstruction except the collimator between the detector and sample was not present. As shown in Figure 27, the reconstructed tomographic image was extremely blurred, even with the noise filter applied. It is suspected that this is due to high-energy gamma-ray contamination and low neutron count rates. Despite the relative gamma-ray insensitivity of the GaAs array [25,35], the 240,000:1 gamma to neutron ratio from the Sb./Be source [4] and low epithermal neutron detection efficiency decrease neutron count rates to below that of the background gamma-rays. Improved Sb/Be source designs and investigations into higher efficiency neutron conversion layers have been developed in order to decrease this affect. Figure 28 shows the reconstructed image with a threshold value of 150, arbitrarily shown to highlight the edges of the steel annulus. The equipment arrangements

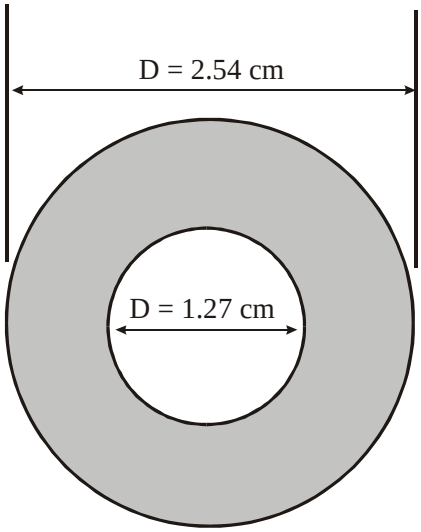

used for the imaging are shown in Figures 29-31.

Figure 26: Schematic drawing of steel cylinder sample imaged using the Sb/Be epithermal neutron source.

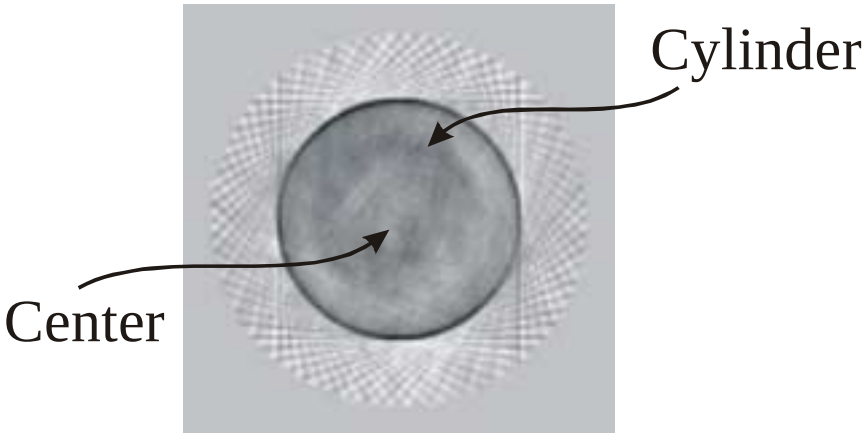

Figure 27: Reconstructed image of steel cylinder sample using a Shepp & Logan filter.

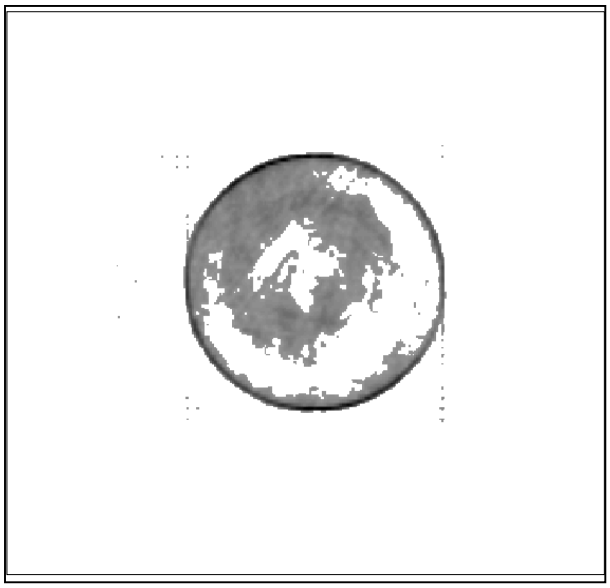

Figure 28: Reconstructed image of steel cylinder sample in an epithermal neutron beam with a threshold value of 150.

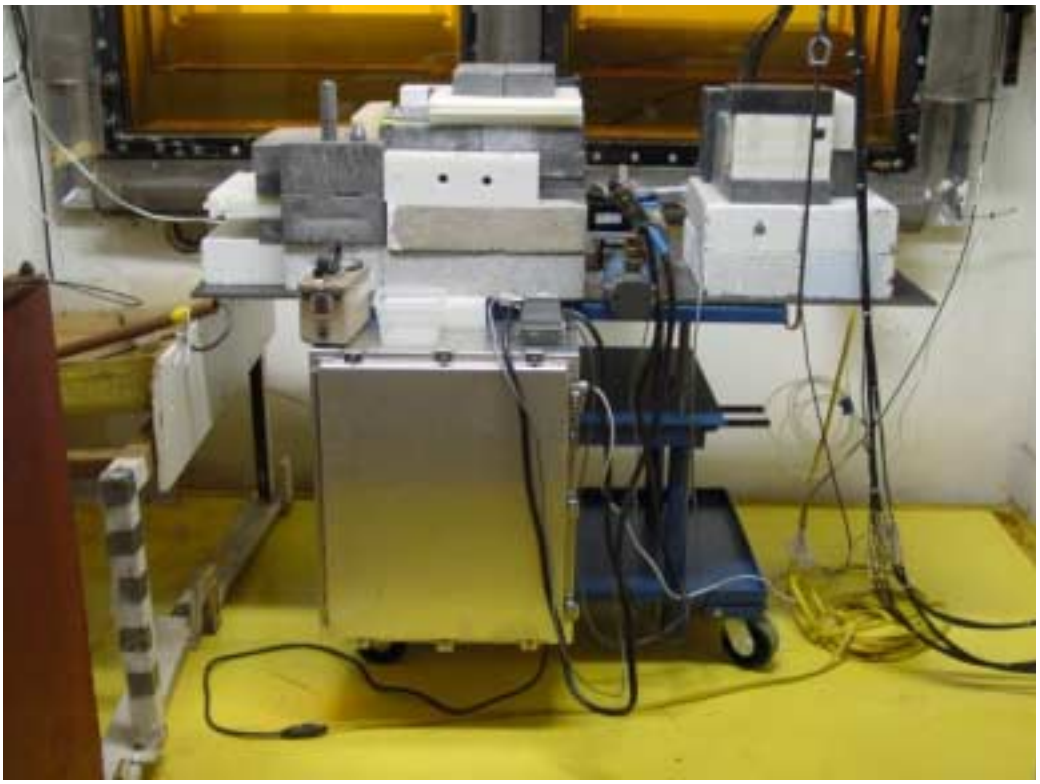

Figure 29: The experimental arrangement used for operating the detector array. The detector box is located on the right within the lead and cinder block shielding.

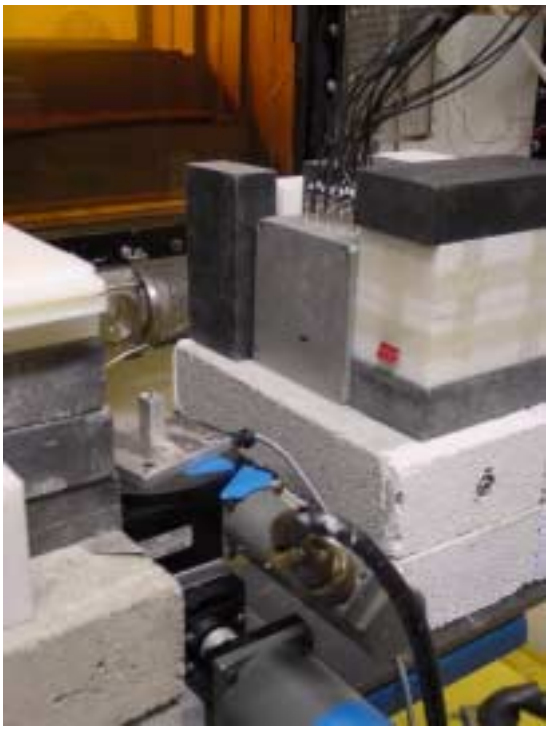

Figure 30: Another view of the detector box.

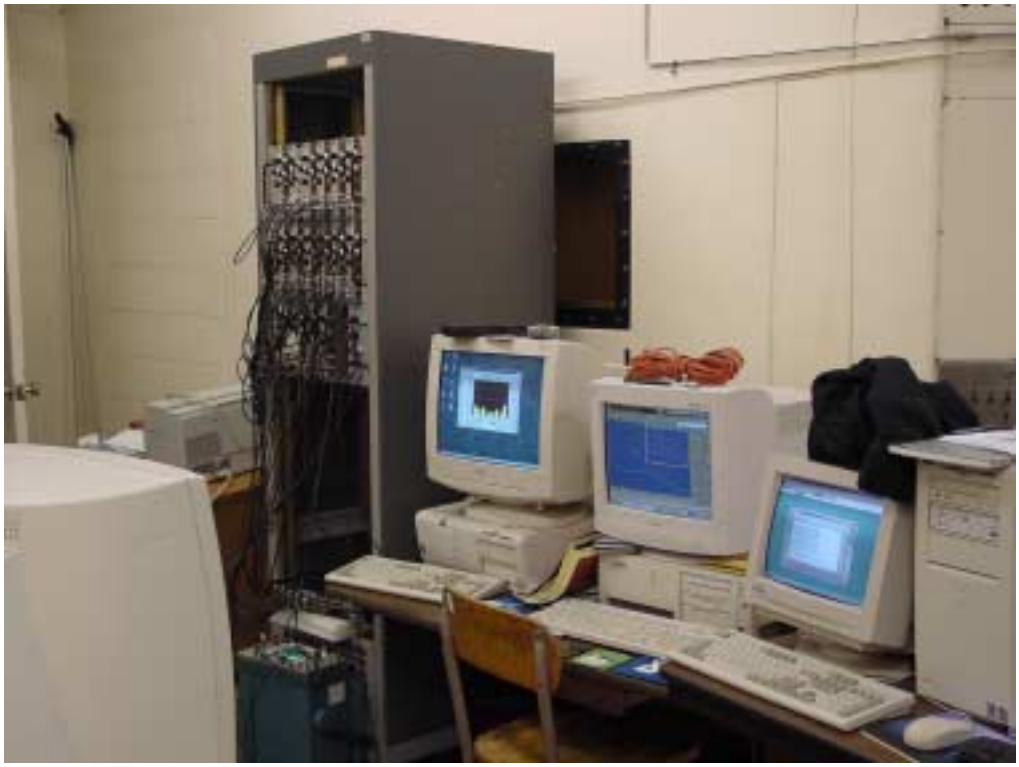

Figure 31. The NIM electronics, SCA, amplifiers and computers used to operate the pixel detectors.

2. Compensated pixel designs

Self-biased compensated pixel designs were tested in the beam port of the Kansas State University TRIGA Mark II nuclear reactor (Figure 32). Figures 33 through 34 show sample spectra of the results, in which it is clear that the subtraction routine separates neutron-induced events from gamma ray induced events.

Figure 33 shows the results from a Gd-coated device. Natural Gd is attractive as a neutron reactive coating due to its high thermal neutron absorption cross section (46,000 barns). Unfortunately, the radiation emissions from neutron interactions in Gd produce relatively low energy reaction products, generally lower than 200 keV, which are emitted as conversion electrons and gamma rays. Hence, in a mixed gamma ray field, it can be difficult to discern whether a radiation interaction event was induce by a neutron or was a direct interaction from a gamma ray in the mixed radiation beam. Figure 33 demonstrates that the compensated pixel method is a viable design that can be used to discern between neutron and gamma ray induced events.

Figure 34 shows the results from a ^{10}B-coated device in a typical mixed gamma ray and neutron beam. Here it is clear why the self-biased design in significant, since very little gamma ray interference is observed. The main reason being the diminutive depletion region absorbs very little gamma ray contamination, but efficiently absorbs the heavy charges particle reaction products from the $^{10}B(n,\alpha)^{7}Li$ reactions. Again, it is easy to discern between gamma ray induced and neutron induced events. Figure 35 shows the results from a ^{10}B-coated device in a mixed gamma ray and neutron beam where the gamma ray component is high (1.1 R). Still, the compensated pixel design allows for clear separation of the gamma ray induced and neutron induced events.

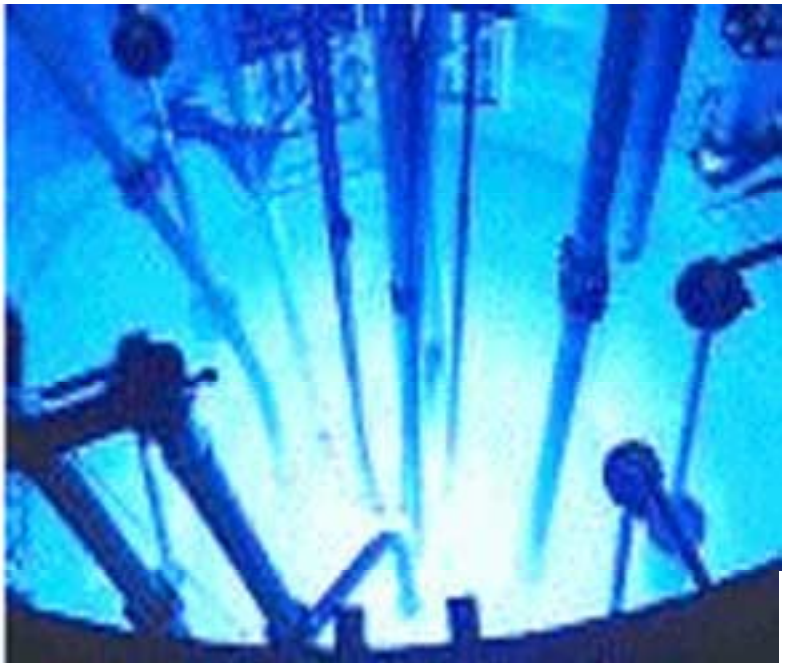

Figure 32: The Kansas State University TRIGA Mark II 250 kW nuclear reactor. The reactor is equipped with four beam ports for collimated neutron beam research.

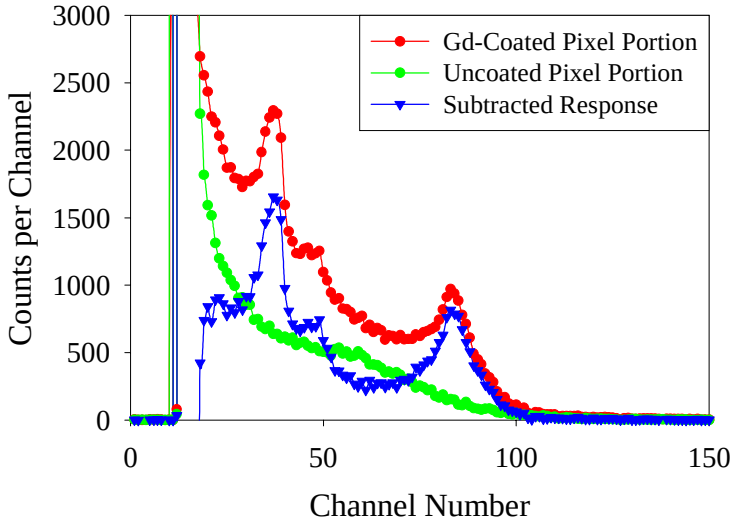

Figure 33: Spectral results from a Gd-coated compensated pixel device operated in a mixed gamma ray and neutron field. Shown are the responses from the coated and uncoated pixel portions and the subtracted result, which reveals the neutron induced spectra.

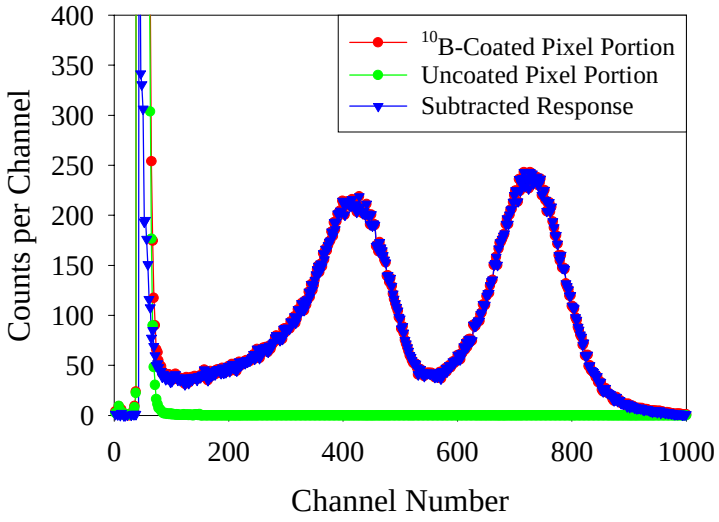

Figure 34: Spectral results from a ^{10}B-coated compensated pixel device operated in a mixed gamma ray and neutron field. Shown are the responses from the coated and uncoated pixel portions and the subtracted result, which reveals the neutron induced spectra.

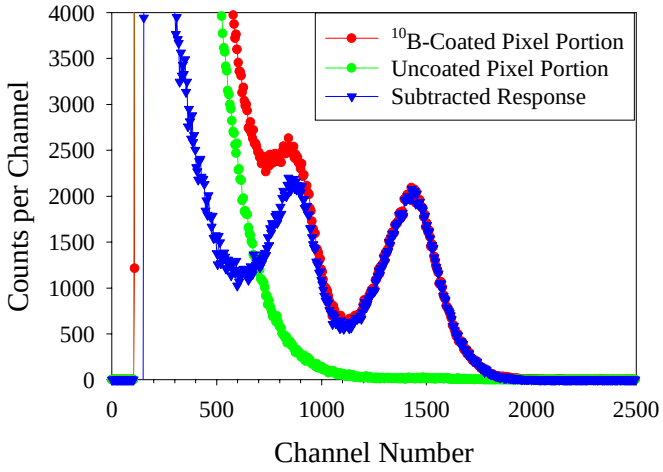

Figure 35: Spectral results from a ^{10}B-coated compensated pixel device in a mixed gamma ray and neutron field where the gamma ray component was exceptionally high. Shown are the responses from the coated and uncoated pixel portions and the subtracted result, which reveals the neutron induced spectra. The subtraction technique easily separates the gamma ray and neutron induced signals.

References:

1. W. Price, *Nuclear Radiation Detection*, 2nd Ed. (McGraw-Hill, New York, 1964).

2. P. Convert, *Position-Sensitive Detection of Thermal Neutrons* (Academic Press, New York, 1983).

3. N. Tsoulfanidis, *Measurement and Detection of Radiation*, 2nd Ed. (Taylor and Francis, New York, 1995).

4. G.F. Knoll, *Radiation Detection and Measurement*, 3rd Ed. (Wiley, New York, 2000).

5. D.I. Garber and R.R. Kinsey, *BNL 325: Neutron Cross Sections*, 3rd Ed., Vol. 2, Curves (Brookhaven National Laboratory, Upton, 1976).

6. V. McLane, C.L. Dunford and P.F. Rose, *Neutron Cross Sections*, Vol. 2 (Academic Press, San Diego, 1988).

7. B. Feigl and H. Rauch, "Der Gd-Neutronenzähler," Nucl. Instr. and Meth., 61, pp. 349-356, 1968.

8. T. Aoyama, Y. Oka, K. Honda and C. Mori, "A Neutron Detector Using Silicon PIN Photodiodes for Personal Neutron Dosimetry," Nucl. Instr. and Meth., A314, pp. 590-594, 1992.

9. A. Mireshghi, G. Cho, J. Drewery, T. Jing, S.N. Kaplan, V. Perez-Mendez, and D. Wildermuth, "Amorphous Silicon Position Sensitive Neutron Detector," IEEE Trans. Nucl. Sci., NS-39, pp. 635-640, 1992.

10. A. Mireshghi, G. Cho, J.S. Drewery, W.S. Hong, T. Jing, H. Lee, S.N. Kaplan and V. Perez-Mendez, "High Efficiency Neutron Sensitive Amorphous Silicon Pixel Detectors," IEEE Trans. Nucl. Sci., NS-41, pp. 915-921, 1994.

11. F. Foulon, P. Bergonzo, A. Brambilla, C. Jany, B. Guizard and R.D. Marshall, "Neutron Detectors Made from Chemically Vapour Deposited Semiconductors," Proc.MRS, 487, pp.591-596, 1998.

12. A.G. Vradii, M.I. Krapivin, L.V. Maslova, O.A. Matveev, A. Kh. Khusainov, V.K. Shashurin, Sov. Atomic Energy, 42, pp. 633-635, 1977.

13. D.S. McGregor, J.T. Lindsay and R.W. Olsen, "Thermal Neutron Detection with $Cadmium_{1-X}Zinc_{X}$Telluride Semiconductor Detectors," Nucl. Instr. and Meth., A381, pp. 498-502, 1996.

14. M.A. Lone, R.A. Levitt and D.A. Harrison, "Prompt Gamma Rays from Thermal-Neutron Capture," Atomic Data and Nuclear Data Tables, 26, pp. 511-519, 1981.

15. J.K. Tuli, “Thermal-Neutron-Capture Gamma Rays,” BNL-NCS-51647 Report, UC-34-C (Brookhaven National Laboratory, Upton, 1983).

16. A.J. Peurrung, “Recent developments in neutron detection,” Nucl. Instr. and Meth., A 443, pp. 400-415, 2000.

17. A. Rose, “Sputtered Boron Films on Silicon Surface Barrier Detectors,” Nucl. Instr. and Meth., 52, pp. 166-170, 1967.

18. I.C. Rickard, “Neutron Spectroscopy in the Energy Range 10-500 keV Using the ^{6}Li Sandwich Detector,” Nucl. Instr. and Meth., 113, pp. 169-174, 1973.

19. R.L. Schulte, F. Swanson and M. Kesselman, “The Use of Large Area Silicon Sensors for Thermal Neutron Detection,” Nucl. Instr. and Meth., A353, pp. 123-127, 1994.

20. D.S. McGregor, J.T. Lindsay, C.C. Brannon and R.W. Olsen, “Semi-insulating Bulk GaAs Thermal Neutron Imaging Arrays,” IEEE Trans. Nucl. Sci., NS-43, pp.1357-1364, 1996.

21. J. Schelten, R. Reinartz, R. Engels, M. Balzhäuser, J. Lauter, W. Schäfer and K.D. Müller, “Position Sensitive Neutron Detection with ^{6}LiF Layers on Silicon Semiconductors,” Nucl. Instr. and Meth., A389, pp. 447-453, 1997.

22. S. Pospisil, B. Sopko, E. Harrankova, Z. Janout, J. Konicek, I Macha, and J. Pavlu, “Si Diode as a Small Detector of Slow Neutrons,” Radiation Protection Dosimetry, 46, pp. 115-118, 1993.

23. M. Campbell, E.H.M. Heijne, J. Kubasta, P. Middelkamp, S. Pospísil, P. Sícho, W. Snoeys and V. Vrba, “Silicon Pixel Devices as a Slow Neutron Precise Position Detector,” Nucl. Instr. and Meth., A395, pp. 457-458, 1997.

24. C. Petrillo, F.Sacchetti, O. Toket, and N.J. Rhodes, “Solid State Neutron Detectors,” Nucl. Instr. and Meth., A 378, pp. 541-551, 1996.

25. D.S. McGregor, R.T. Klann, H.K. Gersch, and Y–H. Yang, “Thin-Film-Coated Bulk GaAs Detectors for Thermal and Fast Neutron Measurements,” Neut. Instr. and Meth., A466, pp. 126-141, 2001.

26. R.T. Klann and D.S. McGregor, “Development of Coated GaAs Neutron Detectors,” *Conference Record of ICONE-8, 8th International Conference on Nuclear Engineering*, April 2-6, 2000, Baltimore, MD USA.

27. D.S. McGregor, S.M. Vernon, H.K. Gersch, S.M. Markham, S.J. Wojtczuk and D.K. Wehe, “Self-Biased Boron-10 Coated High Purity Epitaxial GaAs Thermal Neutron detectors,” IEEE Trans. Nucl. Sci., NS-47, pp. 1364-1370, 2000.

28. D.S. McGregor, R.T. Klann, H.K. Gersch, and J.D. Sanders, "Designs for Thin-Film-Coated Semiconductor Thermal Neutron Detectors," *Conference Record of the IEEE Nuclear Science Symposium*, Nov. 4-9, 2001, San Diego, California, USA.

29. R.D. Evans, *The Atomic Nucleus* (McGraw-Hill, New York, 1955).

30. I. Kaplan, *Nuclear Physics*, 2nd Ed. (Addison-Wesley, Reading, 1962).

31. J.R. Lamarsh, *Introduction to Nuclear Reactor Theory* (Addison-Wesley, Reading, 1972).

32. Sze, S.M., *Physics of Semiconductor Devices,* 2nd Ed. (Wiley, New York, 1981).

33. J.F. Ziegler and J.P. Biersack, SRIM-2000 Code, Version 9 (IBM Company, 1998).

34. H.K. Gersch, D.S. McGregor, and P.A. Simpson, "A Study of the Effect of Incremental Gamma-Ray Doses and Incremental Neutron Fluences Upon the Performance of Self-Biased ^{10}B-Coated High-Purity Epitaxial GaAs Thermal Neutron Detectors," Nucl. Instr. and Meth., 2001, in press.

35. H. Würz, "A Simple Nondestructive Measurement System for Spent-Fuel Management," Nucl. Technol., 95, p. 193, 1991.

36. J.D. Sanders, J.T. Lindsay, and D.S. McGregor, "Development of a GaAs-Based Neutron Tomography System for the Assay of Nuclear Fuel," *Conference Record of the IEEE Nuclear Science Symposium*, Nov. 4-9, 2001, San Diego, California, USA.\

37. H.W. Schmitt, "Determination of the Energy of Antimony-Beryllium Photoneutrons," Nuclear Physics, 20, pp. 220-226, 1960.

38. M. Lalovic and H. Werle, "The Energy Distribution of Antimony-Beryllium Phototneutrons," J. of Nuclear Energy, 24, pp. 123-132, 1977.

39. Y. Ikeda, M. Yokoi, M. Oda, M. Tamaki and G. Matsumoto, "Correction of Scattering Neutron Effects on Neutron CT," Nucl. Instr. and Meth., A377, pp. 85-89, 1996.